



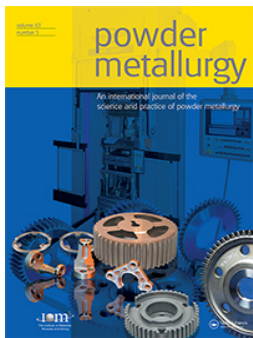
## **Sintering behaviour of compacted water-atomised iron powder: effect of initial state and processing conditions**

Downloaded from: <https://research.chalmers.se>, 2025-07-01 09:21 UTC

Citation for the original published paper (version of record):

Wendel, J., Manchili, S., Hryha, E. et al (2020). Sintering behaviour of compacted water-atomised iron powder: effect of initial state and processing conditions. Powder Metallurgy, 63(5): 338-348.  
<http://dx.doi.org/10.1080/00325899.2020.1833138>

N.B. When citing this work, cite the original published paper.



## Sintering behaviour of compacted water-atomised iron powder: effect of initial state and processing conditions

Johan Wendel , Swathi K. Manchili , Eduard Hryha & Lars Nyborg

To cite this article: Johan Wendel , Swathi K. Manchili , Eduard Hryha & Lars Nyborg (2020) Sintering behaviour of compacted water-atomised iron powder: effect of initial state and processing conditions, Powder Metallurgy, 63:5, 338-348, DOI: [10.1080/00325899.2020.1833138](https://doi.org/10.1080/00325899.2020.1833138)

To link to this article: <https://doi.org/10.1080/00325899.2020.1833138>



© 2020 The Author(s). Published by Informa UK Limited, trading as Taylor & Francis Group



Published online: 03 Nov 2020.



Submit your article to this journal [↗](#)



Article views: 100



View related articles [↗](#)



View Crossmark data [↗](#)

# Sintering behaviour of compacted water-atomised iron powder: effect of initial state and processing conditions

Johan Wendel , Swathi K. Manchili, Eduard Hryha and Lars Nyborg

Department of Industrial and Materials Science, Chalmers University of Technology, Gothenburg, Sweden

## ABSTRACT

Conventional ferrous powder metallurgy relies on uniaxial die-pressing of powder before sintering. The operation causes particle rearrangement and deformation and the initial state of the compact ultimately determines the sintering behaviour. In this study, sintering was investigated for water-atomised iron powder compacted at three different pressure levels, with and without admixed graphite. Electron back-scatter diffraction of the powder and compacts showed a large increase in low-angle grain boundaries after compaction. The sintering of the compacts was investigated by means of dilatometry in hydrogen. The initial compaction strongly influences sintering shrinkage, particularly in the low-temperature, high-diffusivity ferrite region which can account for up to 80% of the recorded shrinkage. Only a small fraction of the total shrinkage originates from the austenite phase, even at high sintering temperatures. However, the ratio of sintering shrinkage in ferrite and austenite changes with compaction pressure, carbon content and heating rate.

## ARTICLE HISTORY

Received 4 June 2020  
Revised 28 September 2020  
Accepted 2 October 2020

## KEYWORDS



Water-atomised iron powder; electron back-scatter diffraction; sintering; dilatometry

## Introduction

In conventional powder metallurgy (PM) of ferrous components, a mix of iron powder, lubricant and graphite is put into a die and subjected to large pressure to force the metal powder particles to acquire a desired shape [1]. After compaction, both the geometry and density of the compacted powder are close to the desired one for the final component. During the compaction step, various levels of particle rearrangement and deformation are introduced with rotational and translational movements of particles at low compaction pressures and additionally elastic and plastic deformation of particles at higher compaction pressures [2–4]. Uniaxial die-compaction also gives rise to green density gradients due to die-wall friction, which may cause distortion and loss of tolerances in the final component during sintering if not controlled properly [5–8]. On a microstructural level, changes in the pore structure are observed in green compacts, with elongated pores present mainly perpendicular to the compaction direction as the contact areas between the powder particles become larger [9,10]. The interparticle contact regions also further change through sintering during which a self-activation effect of the material in regions of increased dislocation density can enhance the sintering process [11–13]. This structural activity and its role during sintering can, in turn, be further affected by several processing parameters such as compaction pressure

and heating rate [12,14]. In this way, the mass transport mechanisms that govern sintering are altered in the interparticle regions, for example by additional diffusion that takes place through dislocation pipes [15–18]. The sintering rates are thereby increased, especially at low temperatures [16,19], which ultimately affects the densification behaviour of the material. Although the annealing of imperfections during sintering indicates a decreasing contribution of the structural activity with temperature and time [12,18,20], further studies are needed to clarify its effect on sintering, especially in relation to geometrical effects [12]. However, it should be emphasised that since the powder used in conventional press and sinter PM of ferrous components is normally coarse, the surface area and driving force for sintering is relatively low, and consequently only small shrinkages are expected.

Apart from the physical conditions required for successful sintering, derived from the compaction of the powder, chemical considerations also have to be taken into account to fully capture the nature of the sintering behaviour [21]. For an effective creation of sinter necks, it is essential to at least partially remove the surface oxides to facilitate the material transport mechanisms involved in sintering [22,23], including carbon dissolution [24]. Several previous studies have neglected the atmospheric influence, sintering instead in vacuum ( $5 \times 10^{-2}$  Pa) or argon [15–20], in

**CONTACT** Johan Wendel  [johan.wendel@chalmers.se](mailto:johan.wendel@chalmers.se)  Department of Industrial and Materials Science, Chalmers University of Technology, Rännvägen 2A, Gothenburg 412 96, Sweden

© 2020 The Author(s). Published by Informa UK Limited, trading as Taylor & Francis Group

This is an Open Access article distributed under the terms of the Creative Commons Attribution License (<http://creativecommons.org/licenses/by/4.0/>), which permits unrestricted use, distribution, and reproduction in any medium, provided the original work is properly cited.

which low-stability iron oxides cannot be effectively reduced at low temperatures [22], which leads to enclosure of oxide fragments [22,25]. The presence of oxides in the interparticle regions, either as a continuous surface oxide layer on powder particles or as discrete oxide particulates or fragments, may affect the mass transport between particles [23,26–28], and thereby also contribute to sintering anisotropy [28]. Consequently, it is believed that additional studies are needed to accurately capture low-temperature sintering shrinkage effects that arise due to compaction, especially for low-alloy steel powder grades containing e.g. Cr, with even higher requirements on sintering atmosphere control [22,25]. Common industrial sintering practice is, therefore, to use hydrogen as a low-temperature reducing component in the processing atmosphere to remove unwanted oxygen and prevent it from interfering with the sinter neck development [22]. Since compaction affects the interparticle regions through the creation of larger contact areas as well as by enclosing oxides and limit access to the process atmosphere [25], there is an important interdependence between particle deformation and sintering atmosphere which will affect the subsequent sintering.

In this study, the sintering behaviour was analysed for two powder size fractions, sieved to below 45 and 75  $\mu\text{m}$ . The initial states of the powder and compacted green samples were studied by means of scanning electron microscopy (SEM) combined with electron backscatter diffraction (EBSD). The microstructural deformation of the metal powder particles was related to the compaction pressure and information about the state of the material before sintering was provided. The sintering behaviour of the compacts was then investigated with dilatometry using a hydrogen atmosphere to reveal effects of the compaction and influence of atmosphere. Both low, 600–800°C, and high, 1350°C, sintering temperatures were used. Reference samples were measured to be able to distinguish the sintering shrinkages from thermal expansion at each step of the sintering cycle. Furthermore, the compaction effects were also investigated in conjunction with a selection of starting material conditions and processing parameters, such as varying compaction pressure, carbon addition and heating rate, to provide an overview of the sintering behaviour of water-atomised iron powder.

## Materials and experimental procedure

Water-atomised iron powder was provided by Höganäs AB, Sweden. The powder is nominally pure iron, but about 0.1 wt-% oxygen and minor amounts of trace elements are typically found. The powder was sieved to two size fractions of maximum 45 and 75  $\mu\text{m}$ , from now on referred to as Fe45 and Fe75,

respectively. For compaction of samples, the powder fractions Fe45 and Fe75 were mixed with 0.6 wt-% LubeE as lubricant and one batch of each powder fraction also had 0.4 wt-% carbon as admixed UF4 natural graphite (Kropfmühl). The compaction was done using a small automatic press at Höganäs AB using compaction pressures of 400, 600, and 800 MPa. Cylindrical samples were produced with 11.3 mm in diameter and 13.5–14.7 mm in height depending on the compaction pressure applied, with a sample mass of approximately 10 g. The green densities of the samples were in the range 86–93% of the theoretical value for iron. Delubrication was done at 450°C in argon (99.999%) for 30 min.

Following compaction and delubrication, analysis of the powder was done by means of SEM using a LEO Gemini 1500 FEG-SEM coupled with EBSD to reveal the deformed structure of the powder particles and compacts. Detailed maps were acquired with a step size of 0.1  $\mu\text{m}$ . The acceleration voltage applied for EBSD analysis was 20 kV with a working distance of 15–20 mm, using Nordlys software (Oxford Instruments). The low- and high-angle grain boundary misorientation limits were set to  $2^\circ < \theta \leq 10^\circ$  and  $\theta > 10^\circ$ , respectively, whereas local misorientation maps (Kernel Average Misorientation, KAM) were created using a kernel exclusion angle of  $2^\circ$ . All EBSD maps were produced with the Channel 5 software (Oxford Instruments).

Sintering of Fe45 and Fe75 compacts was conducted in a Netzsch 402 C push-rod dilatometer. All experiments were conducted in high-purity hydrogen atmosphere (99.9999%) flowing at 100 ml min<sup>-1</sup> to ensure reducing conditions throughout the entire sintering process. Several low-temperature sintering trials were conducted to characterise the sintering in this range. The samples were heated in the range 600–800°C with a heating rate of 30°C min<sup>-1</sup>, held for 1 h, and cooled down to room temperature at 30°C min<sup>-1</sup>. High-temperature sintering experiments were conducted during which samples were heated up to 1350°C, held for 30 min, and then cooled down to room temperature at 30°C min<sup>-1</sup>. The heating rate of the experiments was varied in the range 10–30°C min<sup>-1</sup>. Final sinter densities were determined by the Archimedes water-immersion method.

## Results and discussion

### Powder and green state characterisation

Water-atomised iron powder typically has highly irregular particle morphology with smooth surfaces on a local level on which small oxide particulate features are randomly distributed. Details about the surface chemistry of water-atomised powder grades can be found elsewhere [22,29–31], but it should be noted

that the majority of the surface of the powder particles are covered by a thin iron-rich oxide layer which may interfere with sintering if it acts as a barrier to material movement between particles [22,23,27]. The compressibility of plain iron is good due to the low-yield strength of the material, resulting in green compacts of high density which is a requirement for achieving high sinter densities. A lower compaction density is commonly observed for fine powder fractions due to powder packing effects like higher interparticle friction [32], resulting in a slightly higher porosity for the Fe45 samples. Additionally, the added graphite negatively affects the green density as it takes up volume. With increasing compaction pressure, the powder mixes become increasingly dense. The interparticle contact areas eventually become flattened and increase in size which ultimately leads to a lower increase in density at high compaction pressures [1,2,14,33].

Electron backscatter diffraction was used to give a qualitative indication of the effects of compaction pressure on powder microstructure, especially the plastic deformation in samples compacted at large pressures. This approach has previously been proved useful in studying the microstructure of uniaxially compacted samples [14]. Figure 1(a–f) shows microstructures of green samples depicted as grain boundary maps (left column) and KAM maps (right column) with the compaction direction vertical in the figure. The top row shows the maps for plain powder that is polished, whereas the middle and bottom rows show polished green microstructures of samples from the midsections after being compacted at 400 and 800 MPa, respectively. The grain boundaries of the grain boundary maps are defined as having a degree of misorientation, ( $\theta$ ), of  $2^\circ < \theta \leq 10^\circ$  and  $\theta > 10^\circ$  for low- and high-angle grain boundaries, respectively. A collection of low-angle grain boundaries within a region can represent walls or arrays of dislocations, allowing for a convenient way of representing the deformation [34]. From the left column of Figure 1 it is seen that plain, non-compacted powder is virtually free of low-angle grain boundaries (1a), whereas the compacts show a higher concentration (1c and 1e). The deformation of particles is then clearly not uniform but is confined to certain areas, mainly localised in the vicinity of inter-particle contact regions, i.e. near the edges of the particles. Consequently, smaller particles or small sections of larger particles will have a larger fraction of their total volume deformed than large particles. There is thus a particle size dependence of the deformation. The deformed regions with an increased amount of low-angle grain boundaries, indicating an increased dislocation density, will then start to recover and recrystallise at some elevated temperature during the sintering process. This will act to refine the grain structure of the particles on a

local level, particularly at the edges of the particles, where they are in contact with other particles in the green compact. During the subsequent sintering, the increased grain boundary and dislocation density in these areas is likely going to affect the magnitude of mass transfer and thus sintering by an enhancement of grain boundary and dislocation pipe diffusion as the atoms can easily diffuse in the fine-grained recrystallised inter-particle regions. Apart from the grain boundary structure, there is also evidence of small ( $\theta < 2^\circ$ ) misorientations across the microstructure, see the right column of Figure 1 depicting the KAM maps. These maps can capture small lattice rotation and strain effects and highlight local differences between regions in the microstructure [35], with the small strains in this case typically localised to the particle edges and in the interparticle contact regions. However, the compacted samples also show relatively large intra-granular and intra-particle strains compared to the un-deformed powder, indicating that the deformation effects traverse the entire particle even if not recorded as low- or high-angle grain boundaries. Previous investigations, utilising EBSD to analyse green compacts, also highlight differences in particle boundary orientations where contacts, perpendicular to the compaction direction, have a larger concentration of dislocations than contacts parallel to the compaction direction [14,19]. No significant difference between samples compacted at 400 and 800 MPa could be observed in this investigation, but such a comparison would require an in-depth EBSD analysis.

### Low-temperature sintering behaviour

The initial stages of sintering were investigated by performing a series of low-temperature isothermal sintering trials in the range 600–800°C, see Figure 2(a–c). Based on the bulk chemical composition of the powder, i.e. nominally pure iron powder, the bcc structure of ferrite is expected up to the ferrite to austenite transformation temperature of around 910°C. The self-diffusion coefficient of iron in high-purity iron decreases dramatically from  $4.5\text{E-}11\text{ cm}^2\text{ s}^{-1}$  at around 900°C [36,37] to  $5.1\text{E-}13\text{ cm}^2\text{ s}^{-1}$  at 970°C [36]. At the transformation temperature, the diffusion coefficient was reported to be 660 times higher in  $\alpha$ -Fe than that of  $\gamma$ -Fe [36]. Only at approximately 1200°C is the diffusion coefficient in austenite similar to the one at 900°C in ferrite [37], highlighting the significant influence of the phase on diffusion. In addition, the diffusion coefficients (both grain boundary and volume) have also been shown to be influenced by the magnetic transition at the Curie point ( $\sim 770^\circ\text{C}$ ), as well as by the presence of impurity elements [37,38]. Consequently, the sintering activity is



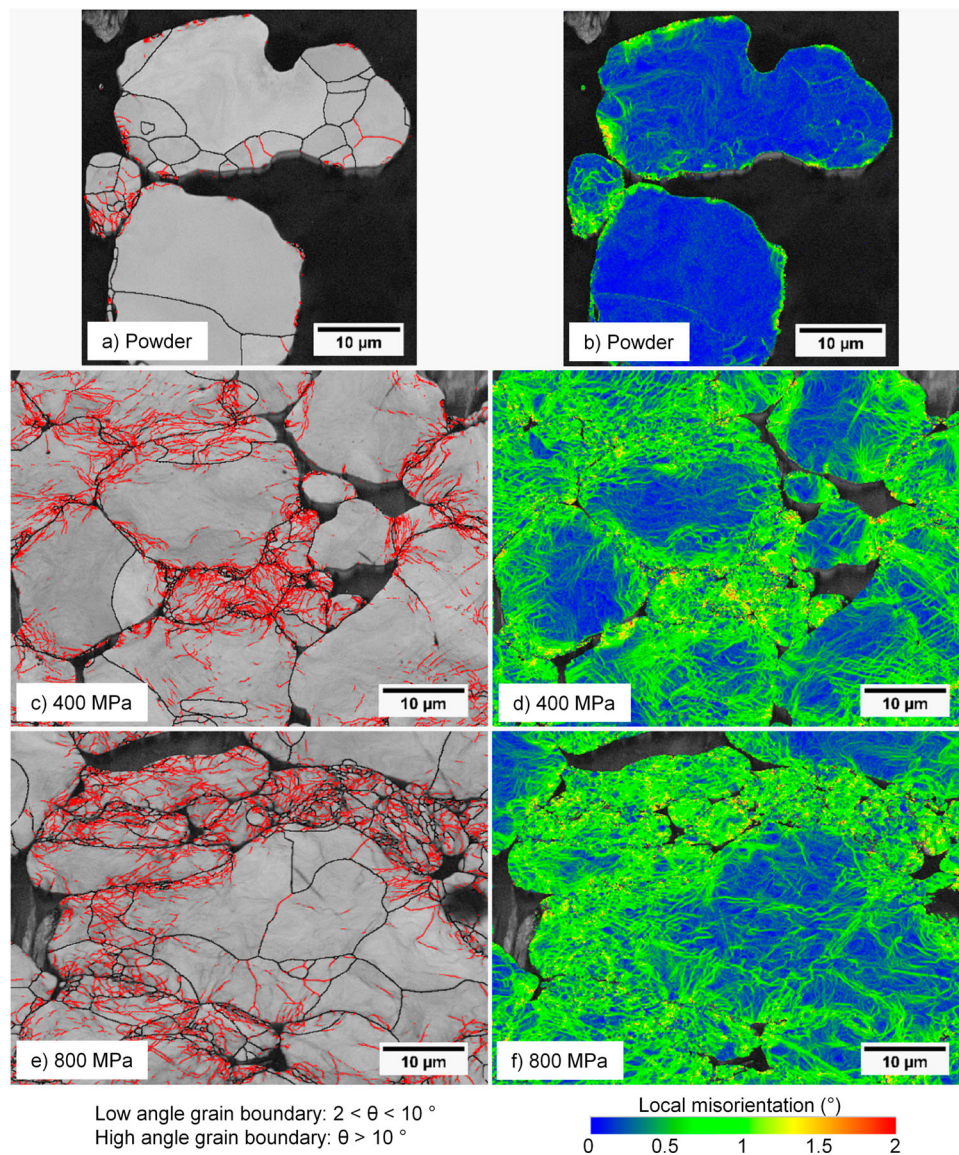


**Figure 1.** EBSD maps depicting the deformation effects of plain powder and green samples compacted at 400 and 800 MPa, respectively. Left column (a, c, e): Grain boundary maps with low-angle grain boundaries as red lines and high-angle grain boundaries as black lines. Right column (b, d, f): KAM maps illustrating the prevalence of small ( $\theta < 2^\circ$ ) misorientations.

expected to be relatively large in the low-temperature ferrite region.

From the dilatometry experiments in Figure 2, it is seen that at 600°C (2a), only small amounts of shrinkage take place for all samples regardless of compaction

pressure. At 700°C (2b), the resulting shrinkages begin to deviate from each other with the sample compacted at the highest compaction pressure producing the largest shrinkage. This trend continues at 800°C (2c), where shrinkage increases up to three times than

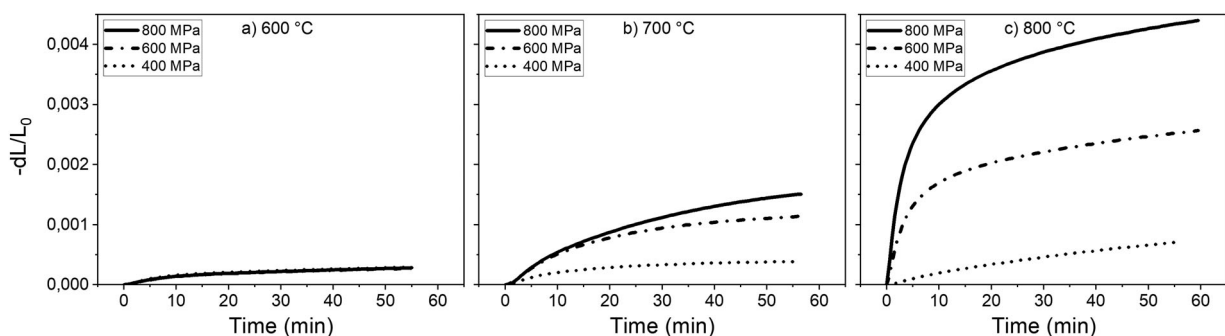


**Figure 2.** Low-temperature isothermal sintering of samples compacted at three different pressures and sintered at different temperatures; (a) 600°C, (b) 700°C, (c) 800°C.

that at 700°C. Larger differences, between the isothermal shrinkages for samples compacted at different compaction pressures, become increasingly evident at elevated temperatures. The sample compacted at 400 MPa shows only slight shrinkage even at 800°C, similar to the shrinkage recorded at 600°C. The low compaction pressures mean that the particles are mainly subjected to rotational and translational movements during compaction, as explained previously, but plastic deformation cannot be ruled out [4,14], as also indicated in Figure 1. However, the resulting cross-sections of the interparticle regions are relatively small with a comparatively small sintering response and no significant effect from the deformation-enhanced diffusivity can be expected. Samples with higher initial green densities, i.e. with larger interparticle contact areas and more pronounced particle deformation, will exhibit much larger shrinkages due to the increase in geometrical factors that are further accentuated by the increase in temperature [12,14,18,19]. It must be emphasised that many of the previous findings, see e.g. [14], disregard the likely effect of the processing atmosphere on densification, so a direct comparison of the magnitude of shrinkages is difficult. Nevertheless, a similar trend was observed [14].

Fracture surfaces of samples sintered at 700°C can be seen in Figure 3(a–d). Samples compacted at 400 MPa (3a) are initially less deformed on a particle level, which translates into lower sintering shrinkage. Consequently, the sinter necks are not as well developed as for samples compacted at higher pressures, where larger interparticle necks can be seen. It is important to note that some neck formation is observed in all cases, which indicates removal of

the iron oxide layer by hydrogen. It is also likely that surface diffusion plays a more dominant role in the sintering of the samples compacted at 400 MPa, something which adds strength to the compacts even without densification [39]. Samples compacted at 600 or 800 MPa, see Figure 3(b,c), sinter to a much larger extent and show a larger amount of clear ductile fractures of the broken sinter necks across the particle surfaces with pronounced sinter neck formation already at these low temperatures.

Previous investigations of these sintering effects at low temperature have mostly been conducted in vacuum conditions [14–19], which can have a profound effect on the measured sintering shrinkage. As discussed previously, a hydrogen-containing atmosphere will facilitate reduction of the surface oxide layer at around 400°C for plain water-atomised iron powder [31]. This ensures that the powder particles are in direct metal–metal contact with each other, thereby enabling the mass transport of metal atoms into the growing sinter neck regions. The fracture surface of a sample sintered at 700°C in nitrogen, see Figure 3(d), does not indicate the presence of any major sinter neck formation. Additionally, the surface oxide layer morphology is changed, indicating a more pronounced surface oxidation in the absence of a strong reducing agent. The result will be similar if a  $\sim 10^{-2}$  Pa vacuum is used as iron oxides do not dissociate under these conditions at low temperatures [40]. This result emphasises the importance of the oxide layer reduction in order to ensure metal–metal contacts between powder particles to allow sintering to take place. Only when this condition is fulfilled the actual kinetics of the sintering process can be revealed.

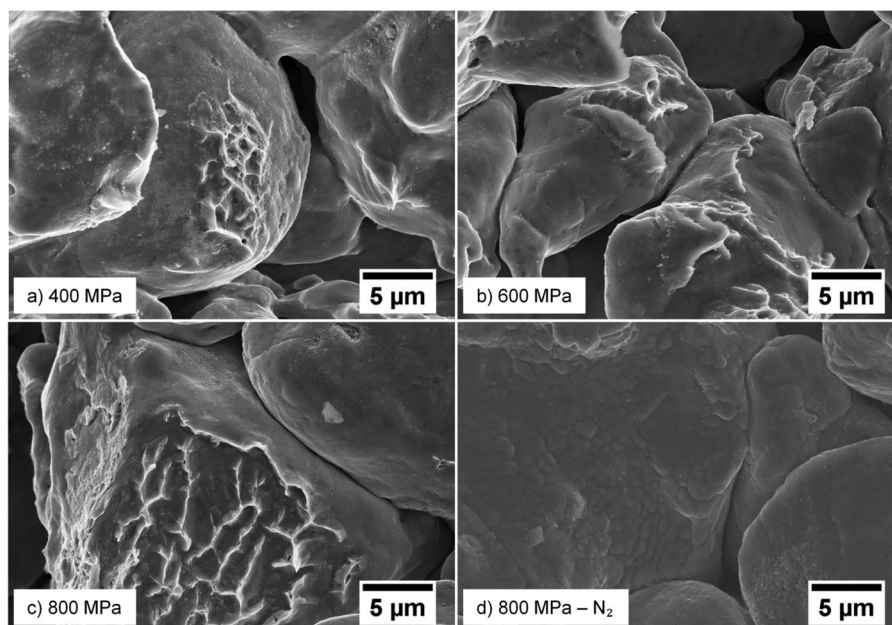


**Figure 3.** Fractographic images of compacts sintered at 700°C: (a) 400 MPa, (b) 600 MPa, (c) 800 MPa, (d) 800 MPa, N<sub>2</sub>.



This reasoning also applies to an industrial setting when sintering is typically accompanied by reducing agents; hydrogen, carbon monoxide or graphite that can reduce the oxide layers between the metal powder particles.

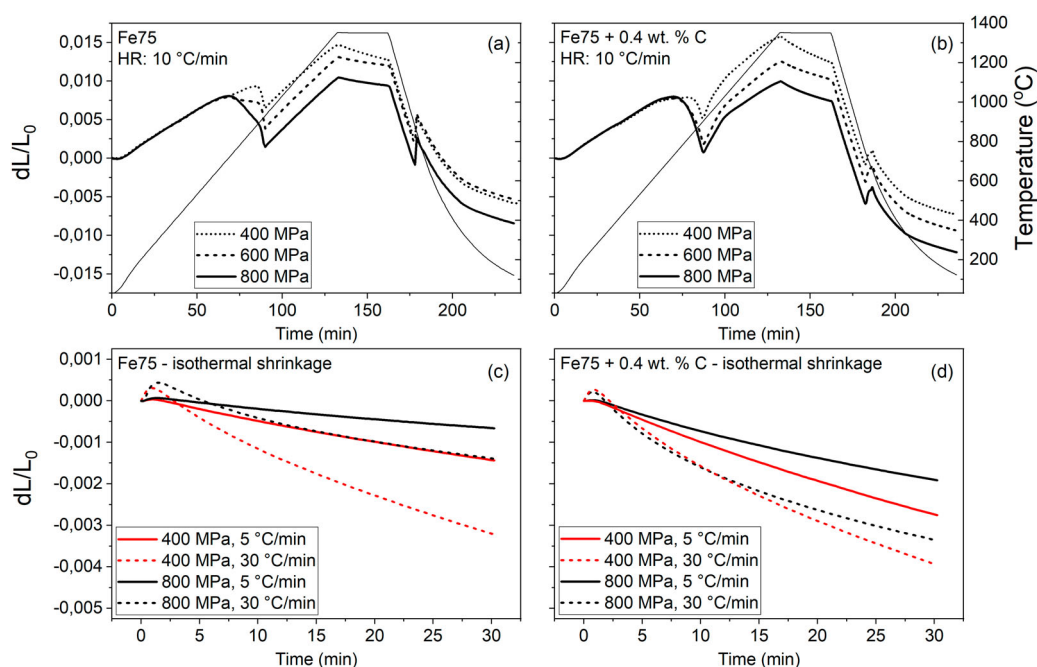
### Full cycle sintering behaviour

The sintering experiments performed at low temperatures do not reflect an industrial sintering cycle, but effectively only capture the initial effects during a real sintering heating stage. However, they can become relevant in revising industrial sintering cycles to improve densification. Full sintering experiments were, therefore, conducted using several different starting conditions and process parameters, see Figure 4(a–d) showing dilatometric results for samples of Fe75 and Fe75 + 0.4 wt-% C at various pressures and heating rates. The results from Fe45 and Fe45 + 0.4 wt-% C samples are omitted here, but the same trend as the Fe75 samples is followed however with a slightly increased amplitude in shrinkage due to the smaller particle size. The final sintering temperature was 1350°C and all sintering cycles were done in a pure hydrogen atmosphere to ensure complete reduction of all relevant oxides. Note that while the chosen sintering temperature is well above the industrial sintering practice of 1120–1250°C, the present results cover a broader range of solid-state sintering of iron powder that is of interest when depicting sintering kinetics.

Figure 4(a) shows the influence of compaction pressure on the sintering shrinkages of the plain

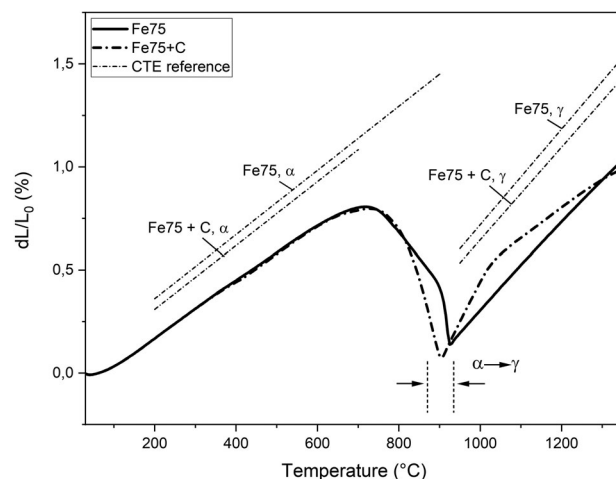
Fe75. It can be seen that the high green density significantly improves the total shrinkage. A detailed analysis of the dilatometry curves shows that most of the shrinkage takes place in the upper temperature of the ferrite region, just below the  $\alpha \rightarrow \gamma$  transformation where the diffusivity in the ferrite is at high. The altered initial state of the highly compacted samples, in terms of increased proximity and coordination number of powder particles, and thus large interparticle contacts, also plays a major role when determining the shrinkage. The strong effect of pressure on sintering in the ferrite region confirms that the magnitude of shrinkage is directly connected to the improved mass transport between the powder particles. Consequently, an improved configuration of powder particles, together with the fast diffusion rates in ferrite, strongly affects the sintering shrinkages [14,15,18,19].

Figure 4(b) shows the effects of adding carbon, as graphite, to the powder before compaction for samples sintered with a heating rate of 10°C min<sup>-1</sup>. Despite the very low solubility of carbon in ferrite, there is a visible effect recorded by the dilatometer in terms of a slight shifting downwards in temperature of the shrinkage close to the transformation. Considering that sintering is done in high-purity hydrogen, the surface oxide layers are removed at relatively low temperatures; this ensures the presence of pure metal surfaces in the upper ferrite region allowing for graphite dissolution and sintering. The dilatometer response can, therefore, be partly explained by a small amount of graphite being dissolved in the ferrite matrix at low temperatures that upon further heating promotes the formation of austenite, thus leading to a blurrier



**Figure 4.** Fe75 sintering cycle matrix. (a) Varying compaction pressure at 10°C min<sup>-1</sup>, (b) with added carbon. (c) Isothermal shrinkage at 1350°C for four sintering conditions, (d) with added carbon.





**Figure 5.** Sintering curves of Fe75 and Fe75+C compacted at 800 MPa and heated at  $10^{\circ}\text{C min}^{-1}$ . The CTE references are included as dotted lines.

$\alpha \rightarrow \gamma$  transformation, c.f. Figure 5. However, it should be stressed that significant carbon dissolution is possible only after the removal of the surface oxide layer and after the material is transformed into austenite [24,41], again emphasising the importance of the oxide layer reduction not only for sinter neck development but also for carbon dissolution. At higher temperatures, the sintering curves initially follow the coefficient of (linear) thermal expansion (CTE) of Fe75+C samples, but due to rapid carbon dissolution in the iron matrix above  $1000^{\circ}\text{C}$  [24,41], the melting temperature is lowered. At a given temperature, the Fe75+C samples will then experience a higher homologous temperature ( $T/T_m$ ) and the sintering curve shows progressive shrinkage at elevated temperatures at a higher rate than for the plain iron samples. This leads to a relatively larger shrinkage in the austenite region for the carbon-containing samples, as shown by the comparison to plain samples in Figure 5.

Figure 4(c,d) shows the isothermal sintering shrinkages for samples prepared using different compaction pressures and different heating rates. The figures illustrate that low compaction pressures lead to large isothermal shrinkages, which are particularly pronounced in the case of plain iron powder. Additionally, high heating rates seem to allow for larger isothermal shrinkages which is believed to be caused by a conservation of sintering driving forces to high temperatures. High heating rates have, in this way, been shown to diminish the contribution of structural activity to sintering in favour of geometrical effects [12]. The effect of carbon addition is also clearly seen where larger shrinkages are recorded compared to plain iron samples. This is related to the melting temperature being lowered by the dissolved carbon, causing diffusion rates and sintering activity to increase as the homologous temperature ( $T/T_m$ ) will be higher.

To distinguish between sintering shrinkages taking place in different regions of the sintering cycle, each dilatometer curve was separated into three principal parts; the (i) ferrite, (ii) austenite and (iii) isothermal sections, similar to previous analyses of dilatometric curves [6,14]. The total shrinkage was taken as the sum of the shrinkages in these regions. The shrinkages in ferrite and austenite ranges were taken from the heating stage of the sintering curve, as negligible amounts of shrinkage were assumed to occur during cooling. To evaluate the shrinkage in each region, the sample sintering curves were compared to the CTE values evaluated from two reference samples of Fe75 and Fe75+C, giving the predicted expansion of a solid sample during heating, see Figure 5. The reference samples were sintered multiple times in order to minimise any influence from sintering on the CTE values, which were then acquired as the average values in  $200\text{--}900$  and  $200\text{--}700^{\circ}\text{C}$  for Fe75 and Fe75+C in ferrite, respectively, and  $950\text{--}1250^{\circ}\text{C}$  for expansion in austenite. The CTE values were determined to be approximately  $15.6$  and  $15.5 \text{ E-6 K}^{-1}$  for expansion in ferrite and  $23.2$  and  $22.5 \text{ E-6 K}^{-1}$  for expansion in austenite, for Fe75 and Fe75+C samples, respectively, see Figures 5 and 6. Table 1 shows the results of the analysis. It should be noted that there are potential difficulties in determining the onset of the ferrite-austenite transformation as the end of the ferrite region is subject to large sintering shrinkage overlapping with the contraction of the transformation. In addition, the partial dissolution of graphite close to the particle edges, as explained previously, will further distort the ferrite-austenite transformation. The predicted expansion in ferrite is calculated from  $200^{\circ}\text{C}$  to the onset of the  $\alpha \rightarrow \gamma$  transformation. The shrinkage from the dilatometer curve in this range is then subtracted from the expansion to yield the real ferrite shrinkage. The predicted expansion in austenite is calculated from  $950$  to  $1250^{\circ}\text{C}$  and the recorded shrinkage is

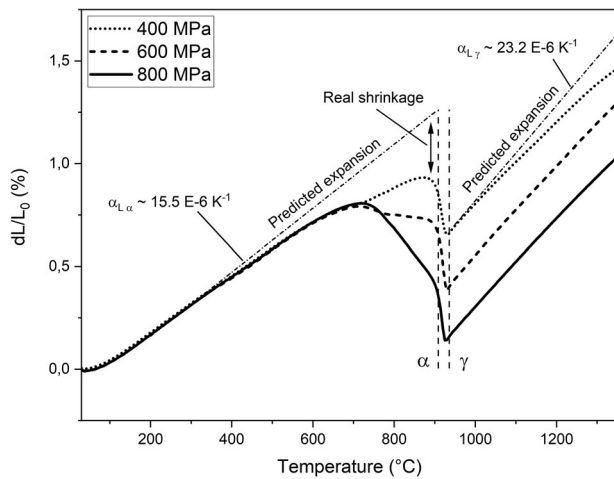


**Figure 6.** Sintering curves of Fe75 and Fe75+C compacted at 800 MPa and heated at 10°C min<sup>-1</sup>. Methodology for determining the sintering shrinkage in each region.

then subtracted from the expansion to yield the real austenite shrinkage. Since no expansion occurs during the isothermal section, the shrinkage values can be extracted directly.

A summary of these calculations is illustrated in Figure 6 in which Fe75 samples, compacted at three different pressures, are analysed. At around 500°C the sintering curves start deviating noticeably from the predicted linear expansion governed by the inherent CTE. At around 700°C, the curves then start deviating from each other, in line with the low-temperature experiments performed at this temperature. The difference is enhanced by further increasing the temperature up to the transformation temperature at ~910°C. At just before the transformation, the compaction effect on sintering is most dramatic, whereas the sintering is essentially halted after the transformation. The crystallographic dependence, on the diffusion coefficients of grain boundary and volume diffusion, is clearly seen, and the densifying diffusion mechanisms become largely inactive. Consequently,

the majority of the heating stage in the austenite phase is characterised by a linear expansion with temperature, indicating that only thermal expansion is active, and no sintering shrinkage is taking place. Approaching the sintering temperature of 1350°C, there is a slight shrinkage in the isothermal section of the sintering curve. The magnitude of this shrinkage is greater for samples compacted at low pressure, which indicates that the more open structure of the lightly sintered material can accommodate larger shrinkage. This is the reverse behaviour compared to the compaction effect of sintering that takes place in the high-diffusivity ferrite region. The procedure was applied on all sintering curves and the result is summarised in Table 1.

As indicated in Figures 5 and 6 and further shown in Table 1, large parts of the measured shrinkages take place in the ferrite region. A similar trend was noted elsewhere [14], but refers to experiments conducted in argon. However, as mentioned previously, this is believed to not represent the relevant industrial case when low temperature reduction is enabled by hydrogen. Adding carbon allows for additional shrinkage in the austenite region where plain iron is normally less active. This is illustrated in Figure 7(a,b) where Fe75 and Fe75 + C samples are compared with respect to the fractional shrinkage that takes place in each region. The effect is especially prominent for plain samples compacted at high pressures where over 80% of the total shrinkage takes place in ferrite. At low compaction pressures, the austenite part of the heating stage and the isothermal sintering hold will be increasingly important. For carbon-containing samples, the ferrite shrinkage still has the largest effect, but the austenite region contributes more to the overall sintering shrinkage. With lowering final sintering temperatures, the austenite/isothermal shrinkages will also diminish accordingly, thus making the ferrite shrinkage even more dominant.

**Table 1.** Sintering shrinkages in different regions of Fe45, Fe45 + C, Fe75 and Fe75 + C samples.

Region/sample	Sintering shrinkages (%) measured by dilatometry								
	400, HR5	400, HR10	400, HR30	600, HR5	600, HR10	600, HR30	800, HR5	800, HR10	800, HR30
<b>Fe45</b>									
Ferrite	0.34	0.36	0.36	0.60	0.67	0.57	0.98	0.96	0.86
Austenite (excluding iso.)	0.14	0.13	0.06	0.16	0.21	0.04	0.12	0.10	0.07
Isothermal	0.13	0.19	0.28	0.09	0.07	0.18	0.08	0.11	0.19
<b>Fe45 + 0.4 wt-% C</b>									
Ferrite	0.55	0.53	0.53	0.92	0.90	0.82	1.07	0.93	0.88
Austenite (excluding iso.)	0.44	0.28	0.12	0.36	0.29	0.16	0.47	0.45	0.35
Isothermal	0.34	0.43	0.55	0.24	0.33	0.41	0.23	0.33	0.43
<b>Fe75</b>									
Ferrite	0.38	0.38	0.47	0.62	0.59	0.53	0.92	0.88	0.77
Austenite (excluding iso.)	0.20	0.16	0.17	0.10	0.07	0.05	0.10	0.09	0.04
Isothermal	0.14	0.19	0.32	0.07	0.09	0.16	0.07	0.09	0.15
<b>Fe75 + 0.4 wt-% C</b>									
Ferrite	0.54	0.51	0.52	0.90	0.79	0.83	1.10	0.97	0.81
Austenite (excluding iso.)	0.25	0.16	0.05	0.19	0.13	0.01	0.34	0.24	0.20
Isothermal	0.28	0.33	0.39	0.19	0.23	0.28	0.19	0.25	0.34

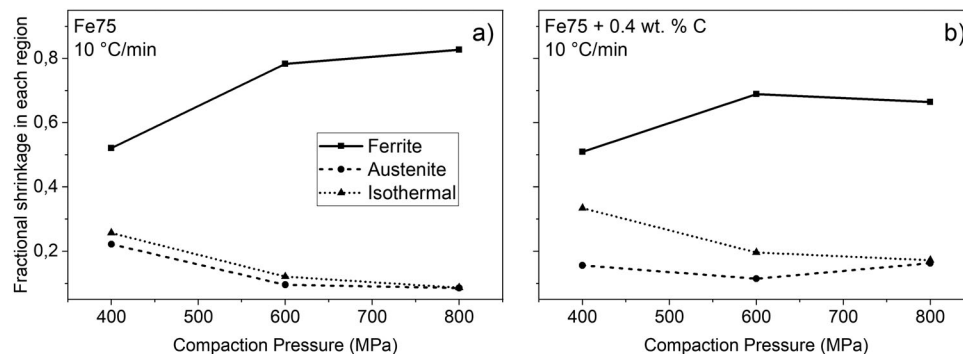


**Figure 7.** Fractional shrinkage in each region of (a) Fe75 and (b) Fe75 + C samples.

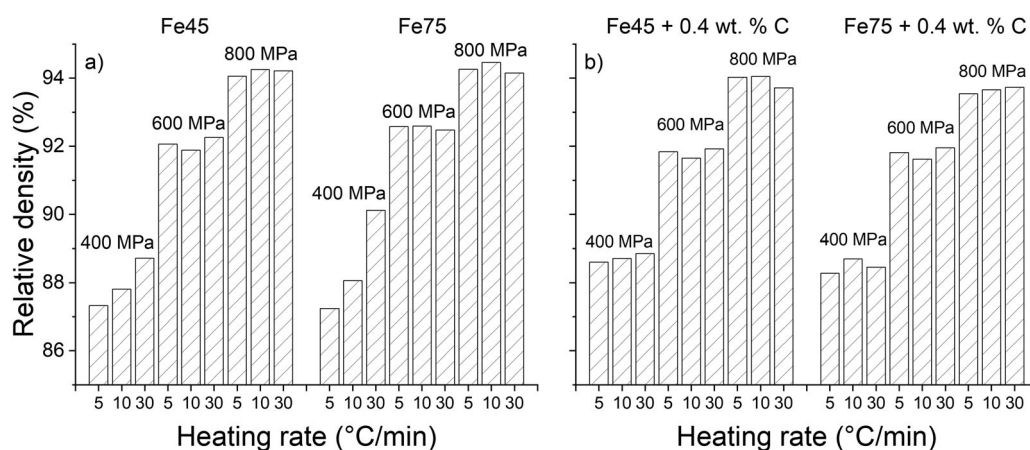


**Figure 8.** Final sintered densities of (a) plain Fe45 and Fe75 and (b) carbon-containing Fe45 and Fe75 samples.

The final densities of the sintered samples can be seen in Figure 8(a,b). It is seen that the densification that takes place is similar between samples of different particle sizes as well as carbon content. The most notable result is the markedly changed density when samples compacted at 400 MPa were subjected to varying heating rates. High heating rates enable the samples to reach high temperatures in austenite faster, where a large amount of shrinkage can take place. This seems beneficial for low green density samples as their low levels of compaction in the green state cannot facilitate large shrinkages in ferrite, and the ferrite should, therefore, be bypassed as fast as possible in favour of high-temperature austenite sintering. Parallel to the investigations in this study, a novel approach of adding nanopowder to water-atomised iron powder has been conducted [42]. These extremely fine powder particles were shown to enhance sintering, particularly at low temperatures where the nanopowder becomes active well before the coarser powder. However, due to the lower compressibility of powder mixes containing nanopowder, the final sinter densities were approximately the same as for samples without nanopowder. Still, the relation between compressibility and sintering activity for finer powder fractions requires further study to reveal their applicability to industrial sintering practice.

## Conclusions

Sintering of ferrous powder compacts is influenced by several factors; the initial state of the powder and green compact, and the processing conditions such as sintering atmosphere. The analyses of plain powder and green samples with EBSD indicate an increase in low-angle grain boundaries and local misorientations in the interparticle contact regions as a result of deformation, with small particles or particle regions having a larger fraction of their total volume deformed. Additionally, intra-particle strains can be observed as a function of the powder particle size. Dilatometry results show increasingly large sintering shrinkages in the range 600–800°C both as a function of isothermal temperature and compaction pressure with a deviation in shrinkages between samples already at 700°C. Consequently, it can be assumed that shrinkage anisotropy begins around these temperatures with relatively larger sintering shrinkages in the direction parallel to compaction than perpendicular to compaction in uniaxially pressed samples. The differences are accentuated as the self-diffusivity of iron increases towards the end of the ferrite region. Complete sintering cycles show that a high compaction pressure gives an overall larger shrinkage, with the effect derived mainly from the large ferrite shrinkage. Addition of

carbon alters the sintering rate in austenite with carbon dissolution, leading to overall larger shrinkages at the isothermal sintering temperature. Despite this, both plain and carbon-containing samples show similar final sintering densities due to lower compressibility. Particle size only marginally affected final sintered densities, likely due to the trade-off where finer powder particles typically show larger sintering shrinkages but are compacted to slightly lower green densities.

## Acknowledgements

This work has been carried out within the project 'Nanotechnology Enhanced Sintered Steel Processing' through support from the Swedish Foundation for Strategic Research under Grant [GMT14-0045] within the programme 'Generic Methods and Tools for Future Production'. Dr Alexander Leicht is greatly acknowledged for assistance with the EBSD measurements and aiding in their interpretation. The authors thank the Area of Advance – Production, at Chalmers University of Technology for support. Höganäs AB, Sweden, is acknowledged for supplying the powder, compaction and scientific cooperation.

## Disclosure statement

No potential conflict of interest was reported by the author(s).

## Funding

This work has been carried out within the project 'Nanotechnology Enhanced Sintered Steel Processing' through support from the Swedish Foundation for Strategic Research [grant number GMT14-0045] within the programme 'Generic Methods and Tools for Future Production'.

## Notes on contributors

**Johan Wendel** is currently working as a Ph.D. student at the Department of Industrial and Materials Science, Chalmers University of Technology, Sweden, with focus on surface chemical and thermoanalytical studies of ferrous powder grades used in powder metallurgy.

**Swathi. K. Manchili** is currently working as a Ph.D. student at the Department of Industrial and Materials Science, Chalmers University of Technology, with focus on nanopowder additions in powder metallurgy.

**Eduard Hryha** received his Ph.D. degree in Materials Engineering in 2008 from the Institute of Materials Research of the Slovak Academy of Sciences, Slovakia. He is currently a full professor at the Department of Industrial and Materials Science, Chalmers University of Technology. His main research activity is devoted to powder metallurgy and additive manufacturing.

**Lars Nyborg** received his Ph.D. degree in Surface Engineering in 1987 from Chalmers University of Technology. He is currently a full professor at the Department of Industrial and Materials Science, Chalmers University of Technology. His main research activity is devoted to surface science, powder metallurgy and additive manufacturing.

## ORCID

Johan Wendel  <http://orcid.org/0000-0003-3659-0498>

## References

- [1] German RM. Sintering theory and practice. New York (NY): John Wiley & Sons; 1996.
- [2] Parilak L, Dudrova E, Bidulsky R, et al. Derivation, testing and application of a practical compaction equation for cold die-compacted metal powders. *Powder Technol.* 2017;322:447–460. DOI:10.1016/j.powtec.2017.09.027.
- [3] Donachie MJ, Burr MF. Effects of pressing on metal powders. *J Met.* 1963;15:849–854. DOI:10.1007/bf03397262.
- [4] Hewitt RL, Wallace W, De Malherbe MC. Plastic deformation in metal powder compaction. *Powder Metall.* 1974;17:1–12. DOI:10.1179/pom.1974.17.33.001.
- [5] Danninger H, Gierl-Mayer C. Advanced powder metallurgy steel alloys. *Adv Powder Metall Prop Process Appl.* 2013; 149–201. DOI:10.1016/0026-0657(92)91807-V.
- [6] Bocchini GF. Influence of process parameters on precision of PM parts. *Powder Metall.* 1985;28:155–165. DOI:10.1179/pom.1985.28.3.155.
- [7] Cristofolini I, Menapace C, Cazzolli M, et al. The effect of anisotropic dimensional change on the precision of steel parts produced by powder metallurgy. *J Mater Process Technol.* 2012;212:1513–1519. DOI:10.1016/j.jmatprotec.2012.02.009.
- [8] Cristofolini I, Pilla M, Rao A, et al. Dimensional and geometrical precision of powder metallurgy parts sintered and sinterhardened at high temperature. *Int J Precis Eng Manuf.* 2013;14:1735–1742. DOI:10.1007/s12541-013-0233-5.
- [9] Lame O, Bellet D, Di Michiel M, et al. Bulk observation of metal powder sintering by X-ray synchrotron microtomography. *Acta Mater.* 2004;52:977–984. DOI:10.1016/j.actamat.2003.10.032.
- [10] Vagnon A, Lame O, Bouvard D, et al. Deformation of steel powder compacts during sintering: correlation between macroscopic measurement and in situ microtomography analysis. *Acta Mater.* 2006;54:513–522. DOI:10.1016/j.actamat.2005.09.030.
- [11] Friedrich E, Schatt W. Sintering of one-component model systems: nucleation and movement of dislocations in necks. *Powder Metall.* 1980;23:193–197.
- [12] Lányi P, Hermel W. Structural activity and shrinkage kinetics in early stages of sintering process. *Powder Metall.* 1981;24:93–100. DOI:10.1179/pom.1981.24.2.93.
- [13] Schatt W, Vetter B, Friedrich E. Non-isothermal shrinkage of compacts. *Powder Metall.* 1991;34:179–182. DOI:10.1179/pom.1991.34.3.179.
- [14] Torresani E. Mechanism of anisotropic shrinkage during sintering of metallic powders [PhD thesis]. University of Trento, 2016.
- [15] Molinari A, Menapace C, Torresani E, et al. Working hypothesis for origin of anisotropic sintering shrinkage caused by prior uniaxial cold compaction. *Powder Metall.* 2012;1–8. DOI:10.1179/1743290112Y.0000000043.
- [16] Molinari A, Bisoffi E, Menapace C, et al. Shrinkage kinetics during the early stage of sintering: the time depending effective diffusion coefficient. *International*



- Powder Metallurgy Congress and Exhibition, Euro PM 2013. 2013. <http://www.scopus.com/inward/record.url?eid=2-s2.0-84924940557&partnerID=tZOtx3y1>.
- [17] Molinari A, Bisoffi E, Menapace C, et al. Shrinkage kinetics during early stage sintering of cold isostatically compacted iron powder. *Powder Metall.* **2014**;57:61–69. DOI:10.1179/1743290113Y.0000000068.
  - [18] Molinari A, Torresani E, Menapace C, et al. The anisotropy of dimensional change on sintering of iron. *J Am Ceram Soc.* **2015**;98:3431–3437. DOI:10.1111/jace.13852.
  - [19] Torresani E, Giuntini D, Zhu C, et al. Anisotropy of mass transfer during sintering of powder materials with pore–particle structure orientation. *Metall Mater Trans A.* **2018**. DOI:10.1007/s11661-018-5037-x.
  - [20] Baselli S, Torresani E, Zago M, et al. Sintering shrinkage of uniaxial cold compacted iron: influence of the microstructure on the anisothermal and isothermal shrinkage of uniaxial cold-compacted iron. *Powder Metall.* **2018**;61:276–284. DOI:10.1080/00325899.2018.1500783.
  - [21] Danninger H, Gierl C, Kremel S, et al. Deoxidation processes during sintering of unalloyed and alloyed PM steels. *Powder Metall Prog.* **2002**;2:125–140.
  - [22] Chasoglou D, Hryha E, Nyborg L. Effect of process parameters on surface oxides on chromium-alloyed steel powder during sintering. *Mater Chem Phys.* **2013**;138:405–415. DOI:10.1016/j.matchemphys.2012.11.074.
  - [23] Ramakrishnan P, Tendolkar GS. Influence of thin oxide films on the mechanical properties of sintered metal-powder compacts. *Powder Metall.* **1964**;7:34–49. DOI:10.1179/pom.1964.7.13.003.
  - [24] Hryha E, Nyborg L, Alzati L. Dissolution of carbon in Cr-prealloyed PM steels: effect of carbon source. *Powder Metall.* **2015**;58:7–11. DOI:10.1179/0032589914Z.000000000191.
  - [25] Hryha E, Nyborg L. Oxide transformation in Cr-Mn-prealloyed sintered steels: thermodynamic and kinetic aspects. *Metall Mater Trans A Phys Metall Mater Sci.* **2014**;45:1736–1747. DOI:10.1007/s11661-013-1969-3.
  - [26] Higgins PK, Munir ZA. Influence of surface oxide layer on sintering process of lead. *Powder Metall.* **1978**;21:188–194. DOI:10.1179/pom.1978.21.4.188.
  - [27] Munir ZA. Surface oxides and sintering of metals. *Powder Metall.* **1981**;24:177–180. DOI:10.1179/pom.1981.24.4.177.
  - [28] Zavaliangos A, Missiaen JM, Bouvard D. Anisotropy in shrinkage during sintering. *Sci Sinter.* **2006**;38:13–25. DOI:10.2298/SOS0601013Z.
  - [29] Chasoglou D, Hryha E, Nyborg L. Effect of sintering atmosphere on the transformation of surface oxides during the sintering of chromium alloyed steel. *Powder Metall Prog.* **2010**;9(2009):141–155.
  - [30] Chasoglou D, Hryha E, Norell M, et al. Characterization of surface oxides on water-atomized steel powder by XPS/AES depth profiling and nano-scale lateral surface analysis. *Appl Surf Sci.* **2013**;268:496–506. DOI:10.1016/j.apsusc.2012.12.155.
  - [31] Wendel J, Shvab R, Cao Y, et al. Surface analysis of fine water-atomized iron powder and sintered material. *Surf Interface Anal.* **2018**;50:1065–1071. DOI:10.1002/sia.6455.
  - [32] Schatt W, Wieters K-P. Powder metallurgy – processing and materials. European Powder Metallurgy Association, shrewsbury: UK, 1997.
  - [33] Hryha E, Dudrova E, Bengtsson S. Influence of powder properties on compressibility of prealloyed atomised powders. *Powder Metall.* **2008**;51:340–342. DOI:10.1179/174329008(286596).
  - [34] Brewer LN, Othon MA, Young LM, et al. Misorientation mapping for visualization of plastic deformation via electron back-scattered diffraction. *Microsc Microanal.* **2006**;12:85–91. DOI:10.1017/S1431927606060120.
  - [35] Wright SI, Nowell MM, Field DP. A review of strain analysis using electron backscatter diffraction. *Microsc Microanal.* **2011**;17:316–329. DOI:10.1017/S1431927611000055.
  - [36] Birchenall CE, Mehl RF. Self-diffusion in alpha and gamma iron. *Jom.* **1950**;2:144–149. DOI:10.1007/bf03398989.
  - [37] Buffington FS, Hirano K, Cohen M. Self diffusion in iron. *Acta Metall.* **1961**;9:434–439. DOI:10.1016/0001-6160(61)90137-7.
  - [38] Iijima Y. Diffusion in high-purity iron: influence of magnetic transformation on diffusion. *J Phase Equilibria Diffus.* **2005**;26:466–471. DOI:10.1361/154770305X66547.
  - [39] Poster AR, Hausner HH. Alpha and gamma phase sintering of carbonyl and other iron powders. *Mod Dev Powder Metall.* **1966**:26–44. DOI:10.1007/978-1-4684-7882-2\_3.
  - [40] Hryha E, Dudrova E, Nyborg L. On-line control of processing atmospheres for proper sintering of oxidation-sensitive PM steels. *J Mater Process Technol.* **2012**;212:977–987. DOI:10.1016/j.jmatprotec.2011.12.008.
  - [41] Hryha E, Nyborg L. Microstructure development in powder metallurgy steels: effect of alloying elements and process variables. *Mater Sci Forum.* **2014**;782:467–472. DOI:10.4028/www.scientific.net/MSF.782.467.
  - [42] Manchili SK, Wendel J, Zehri A, et al. Effect of nano-powder addition on the sintering of water-atomized iron powder. *Metall Mater Trans A Phys Metall Mater Sci.* **2020**;51:4890–4901. DOI:10.1007/s11661-020-05891-1.